Wideband quantitative ultrasonic imaging by time-domain diffraction tomography

T. Douglas Mast
Applied Research Laboratory, The Pennsylvania State University, University Park, Pennsylvania 16802

(Received 3 April 1999; revised 27 August 1999; accepted 30 August 1999)

A quantitative ultrasonic imaging method employing time-domain scattering data is presented. This method provides tomographic images of medium properties such as the sound speed contrast; these images are equivalent to multiple-frequency filtered-backpropagation reconstructions using all frequencies within the bandwidth of the incident pulse employed. However, image synthesis is performed directly in the time domain using coherent combination of far-field scattered pressure waveforms, delayed and summed to numerically focus on the unknown medium. The time-domain method is more efficient than multiple-frequency diffraction tomography methods, and can, in some cases, be more efficient than single-frequency diffraction tomography. Example reconstructions, obtained using synthetic data for two- and three-dimensional scattering of wideband pulses, show that the time-domain reconstruction method provides image quality superior to single-frequency reconstructions for objects of size and contrast relevant to medical imaging problems such as ultrasonic mammography. The present method is closely related to existing synthetic-aperture imaging methods such as those employed in clinical ultrasound scanners. Thus, the new method can be extended to incorporate available image-enhancement techniques such as time-gain compensation to correct for medium absorption and aberration correction methods to reduce error associated with weak scattering approximations.
[S0001-4966(99)04612-3]

PACS numbers: 43.20.Fn, 43.60.Rw, 43.80.Vj, 43.20.Px [ANN]

INTRODUCTION

Quantitative imaging of tissue properties is a potentially useful technique for diagnosis of cancer and other pathological conditions. Inverse scattering methods such as diffraction tomography can provide quantitative reconstruction of tissue properties including sound speed, density, and absorption. However, although previous inverse scattering methods have achieved high resolution and quantitative accuracy, such methods have not yet been incorporated into commercially successful medical ultrasound imaging systems.

Current inverse scattering methods are lacking in several respects with respect to conventional B-scan and synthetic aperture imaging techniques. Previous methods of diffraction tomography, including methods based on the Born and Rytov approximations,[1,2] and higher-order nonlinear approaches,[3,4] have usually been based on single-frequency scattering, while current diagnostic ultrasound scanners employ wideband time-domain signals. The use of wideband information in image reconstruction is known to provide increased point and contrast resolution,[5,6] both of which are important for medical diagnosis.[5,7,8]

Several approaches have been used to incorporate wideband scattering information into quantitative ultrasonic imaging. One group of methods employs time-domain tomography based on Radon-transform relationships that hold (under the assumption of weak scattering) between scattered acoustic fields and the reflectivity or scattering strength of the medium. Pioneering work in this area[9,10] employed measurements of reflectivity in pulse-echo mode, while later studies have incorporated aberration correction[11,12] and multiple-angle scattering measurements.[13,14] A limitation of these methods, however, is that the Radon transform relationship strictly holds only when the medium is insonified by an impulsive (infinite bandwidth) wave. When pulses of finite bandwidth are employed, image quality can degrade significantly.[15]

A number of linear and nonlinear diffraction tomography methods have been implemented using scattering data for a number of discrete frequencies (e.g., Refs. 16–19). Although use of multiple-frequency data provides improvements in image quality, computational requirements for multiple-frequency imaging are typically large because the computational cost is proportional to the number of frequencies employed. To achieve image quality competitive with present diagnostic scanners, together with quantitative imaging of tissue properties, present frequency-domain methods may require solution of the inverse scattering problem for many frequencies within the bandwidth of the transducer employed. This approach thus demands a high computational cost, so that high-quality real-time imaging may not be presently feasible using current frequency-domain inverse scattering methods.

Very few previous workers have investigated direct use of time-domain waveform data for inverse scattering methods analogous to frequency-domain diffraction tomography. Several methods[20,21] have used frequency decomposition of scattered pulses to construct a wideband estimate of the spatial Fourier transform of an unknown medium; after appropriate averaging and interpolation, this transform can be inverted to obtain a wideband Born reconstruction of the medium. A study reported in Ref. 22 has showed that broadband synthetic aperture imaging using linear arrays is closely

related to inverse scattering using filtered backpropagation. A related method, suggested in Ref. 23, provides a time-domain reconstruction algorithm that employs filtered backpropagation of scattered waveforms measured on a circular boundary. However, the time domain reconstruction formula of Ref. 23 yields reconstructions that are less general than multiple-frequency reconstructions obtained using the same signal bandwidth.

Another approach, related both to multiple-frequency methods and direct time-domain methods, has recently been presented.[24] This work extends the eigenfunction method of Ref. 19 to use the full bandwidth of the incident pulse waveform. In the extended method, eigenfunctions and eigenvalues of a scattering operator are computed to obtain a frequency-dependent representation of the scattering medium. Fourier synthesis is then applied to obtain a time-dependent estimate of the medium. A cross-correlation operation removes the time dependence of the estimate as well as its dependence on the waveform employed.

The present paper offers a new approach to wideband quantitative imaging: a time-domain inverse scattering method that overcomes some of the limitations of previous frequency-domain and time-domain quantitative imaging methods. The new method provides tomographic reconstructions of unknown scattering media using the entire available bandwidth of the signals employed. Reconstructions are performed using scattering data measured on a surface surrounding the region of interest, so that the method is well suited to ultrasonic mammography. The reconstruction algorithm is derived as a simple delay-and-sum formula similar to synthetic-aperture algorithms employed in conventional clinical scanners. However, unlike current clinical scanners, the present method can provide quantitative images of tissue properties such as the spatially dependent sound speed. Reconstructions obtained in this manner are equivalent to reconstructions obtained by combining conventional frequency-domain diffraction tomography reconstructions for all frequencies within the signal bandwidth of interest. The current method, however, can be even more efficient than single-frequency diffraction tomography. The method is applicable both to two-dimensional and three-dimensional image reconstruction. The direct time-domain nature of the reconstruction algorithm allows straightforward incorporation of depth- and frequency-dependent amplitude correction to compensate for medium absorption as well as aberration correction methods to overcome limitations of the Born approximation.

I. THEORY

A. The time-domain reconstruction algorithm

An inverse scattering algorithm, applicable to quantitative imaging of tissue and other inhomogeneous media, is derived below. For simplicity of derivation, the medium is modeled as a fluid medium defined by the sound speed contrast function

$$\gamma(\mathbf{r}) = \frac{c_0^2}{c(\mathbf{r})^2} - 1, \tag{1}$$

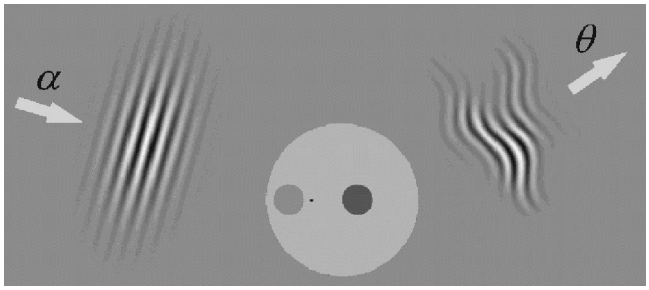

FIG. 1. Scattering configuration. An incident pressure pulse $f(t-\boldsymbol{\alpha}\cdot r/c)$ is scattered by an inhomogeneous medium and the time-domain scattered pressure $p_s(\boldsymbol{\theta},\boldsymbol{\alpha},t)$ is measured at a radius R in the far field.

where c_0 is a background sound speed and $c(\mathbf{r})$ is the spatially dependent sound speed defined at all points $\mathbf{r}$. For the scope of the initial derivation, the medium is assumed to have constant density, no absorption, and weak scattering characteristics; extensions to the reconstruction algorithm that overcome these limiting assumptions are discussed in the following section.

For the model of the scattering medium represented by Eq. (1), the time-domain scattered acoustic pressure $p_s(\mathbf{r},t)$ obeys the wave equation[25]

$$\nabla^2 p_s(\mathbf{r},t) - \frac{1}{c_0^2}\frac{\partial^2 p_s(\mathbf{r},t)}{\partial t^2} = \frac{\gamma(\mathbf{r})}{c_0^2}\frac{\partial^2 p(\mathbf{r},t)}{\partial t^2}, \tag{2}$$

where $p(\mathbf{r},t)$ is the total acoustic pressure in the medium.

The scattering configuration considered here is sketched in Fig. 1. The medium is subjected to a pulsatile plane wave propagating in the direction of the unit vector $\boldsymbol{\alpha}$,

$$p_{\mathrm{inc}}(\mathbf{r},\boldsymbol{\alpha},t) = f(t-\mathbf{r}\cdot\boldsymbol{\alpha}/c_0), \tag{3}$$

where f is the time-domain waveform and c_0 is the background sound speed. The scattered wavefield $p_s(\boldsymbol{\theta},\boldsymbol{\alpha},t)$ is measured at a fixed radius R in the far field, where $\boldsymbol{\theta}$ corresponds to the direction unit vector of a receiving transducer element. (Alternatively, if scattering measurements are made in the near field, the far-field acoustic pressure can be computed using exact transforms that represent propagation through a homogeneous medium.[16])

A general time-domain solution for the wave equation (2), valid for two-dimensional (2D) or three-dimensional (3D) scattering, is then

$$p_s(\boldsymbol{\theta},\boldsymbol{\alpha},t) = \int_{-\infty}^{\infty} \hat{p}_s(\boldsymbol{\theta},\boldsymbol{\alpha},\omega) e^{-i\omega t} d\omega, \tag{4}$$

where $\hat{p}_s(\boldsymbol{\theta},\boldsymbol{\alpha},\omega)$ is a single frequency component of the scattered wavefield,

$$\hat{p}_s(\boldsymbol{\theta},\boldsymbol{\alpha},\omega) \equiv \frac{1}{2\pi}\int_{-\infty}^{\infty} p_s(\boldsymbol{\theta},\boldsymbol{\alpha},t) e^{i\omega t} dt, \tag{5}$$

given exactly by[25]

$$\hat{p}_s(\boldsymbol{\theta},\boldsymbol{\alpha},\omega) = k^2 \hat{f}(\omega) \int \mathrm{G}_0(R\boldsymbol{\theta}-\mathbf{r}_0,\omega) \times \gamma(\mathbf{r}_0)\hat{p}(\mathbf{r},\boldsymbol{\alpha},\omega) dV_0. \tag{6}$$

In Eq. (6), k is the wave number ω/c_0 and $\hat{p}(\mathbf{r}_0,\boldsymbol{\alpha},\omega)$ is the total acoustic pressure associated with the unit-amplitude incident plane wave $e^{ik\boldsymbol{\alpha}\cdot\mathbf{r}_0}$. The integral in Eq. (6) is taken over the entire support of γ in $\mathbb{R}^2$ for 2D scattering or in $\mathbb{R}^3$

for 3D scattering. The free-space Green's function, represented by G_0 in Eq. (6), is[26]

$$G_0(\mathbf{r},\omega)=\frac{i}{4}H_0^{(1)}(kr) \quad \text{for 2D scattering}$$

and (7)

$$G_0(\mathbf{r},\omega)=\frac{e^{ikr}}{4\pi r} \quad \text{for 3D scattering,}$$

where $H_0^{(1)}$ is the zeroth-order Hankel function of the first kind and r is the magnitude of the vector $\mathbf{r}$.

The far-field scattered pressure, when specified for all incident-wave directions $\boldsymbol{\alpha}$, measurement directions $\boldsymbol{\theta}$, and times t, comprises the data set to be used for reconstruction of the unknown medium. The inverse scattering problem, specified by Eq. (6) for a single frequency component, is to reconstruct the unknown medium contrast $\gamma(\mathbf{r})$ using the measured data $\hat{p}_s(\boldsymbol{\theta},\boldsymbol{\alpha},\omega)$.

The starting point for the present time-domain inverse scattering method is conventional single-frequency diffraction tomography. Under the assumption of weak scattering, one can make the Born approximation, in which the total pressure $\hat{p}(\boldsymbol{\alpha},\omega)$ in Eq. (6) is replaced by the plane wave $e^{ik\mathbf{r}\cdot\boldsymbol{\alpha}}$. For scattering measurements made at a radius R in the far field, the linearized inverse problem of Eq. (6) can be then solved for any frequency component using filtered backpropagation,[2,16,27] i.e.,

$$\gamma_B(\mathbf{r},\omega)=\frac{\hat{\mu}(\omega)e^{-ikR}}{\hat{f}(\omega)}\int\int\Phi(\boldsymbol{\theta},\boldsymbol{\alpha})\times\hat{p}_s(\boldsymbol{\theta},\boldsymbol{\alpha},\omega)e^{ik(\boldsymbol{\theta}-\boldsymbol{\alpha})\cdot\mathbf{r}}dS_\alpha dS_\theta, \quad (8)$$

where

$$\hat{\mu}(\omega)=-\sqrt{\frac{kR}{8i\pi^3}},$$

$$\Phi(\boldsymbol{\theta},\boldsymbol{\alpha})=|\sin(\theta-\alpha)| \quad \text{in 2D,}$$

and (9)

$$\hat{\mu}(\omega)=\frac{kR}{4\pi^3}, \quad \Phi(\boldsymbol{\theta},\boldsymbol{\alpha})=|\boldsymbol{\theta}-\boldsymbol{\alpha}| \quad \text{in 3D.}$$

Each surface integral in Eq. (8) is performed over the entire measurement circle for the 2D case and over the entire measurement sphere for the 3D case. Equation (8) provides an exact solution to the linearized inverse scattering problem for a single frequency component of the scattered wavefield $p_s(\boldsymbol{\theta},\boldsymbol{\alpha},t)$. The resulting reconstruction, $\gamma_B(\mathbf{r},\omega)$, has spatial frequency content limited by the ''Ewald sphere'' of radius $2k$ in wavespace.[1]

To improve upon the single-frequency formulas specified by Eq. (8), one can extend the spatial-frequency content of reconstructions by exploiting wideband scattering information. The method outlined here synthesizes a ''multiple-frequency'' reconstruction $\gamma_M(\mathbf{r})$ by formally integrating single-frequency reconstructions $\gamma_B(\mathbf{r},\omega)$ over a range of frequencies ω. A generalized formula for this approach can be written

$$\gamma_M(\mathbf{r})=\frac{\int_0^\infty\hat{g}(\omega)\gamma_B(\mathbf{r},\omega)d\omega}{\int_0^\infty\hat{g}(\omega)d\omega}, \quad (10)$$

where $\hat{g}(\omega)$ is an appropriate frequency-dependent weighting function. In practice, the weighting function $\hat{g}(\omega)$ is chosen to be bandlimited because (for a given set of physical scattering measurements) the frequency-dependent contrast $\gamma_B(\mathbf{r},\omega)$ can only be reliably reconstructed for a finite range of frequencies ω associated with the spectra of the incident waves employed. Thus, the integrands in Eq. (10) are nonzero only over the support of $\hat{g}(\omega)$ and the corresponding integrals are finite.

Using Eq. (8), and making the definition

$$N\equiv 2\int_0^\infty\hat{g}(\omega)d\omega, \quad (11)$$

Eq. (10) can be written in the form

$$\gamma_M(\mathbf{r})=\frac{2}{N}\int_0^\infty\hat{g}(\omega)\frac{\hat{\mu}(\omega)e^{-ikR}}{\hat{f}(\omega)}\int\int\Phi(\boldsymbol{\theta},\boldsymbol{\alpha})\times\hat{p}_s(\boldsymbol{\theta},\boldsymbol{\alpha},\omega)e^{ik(\boldsymbol{\theta}-\boldsymbol{\alpha})\cdot\mathbf{r}}dS_\alpha dS_\theta d\omega. \quad (12)$$

If the frequency weight $\hat{g}(\omega)$ is now specified to incorporate the incident-pulse spectrum $\hat{f}(\omega)$ and to compensate for the frequency- and dimension-dependent coefficient $\hat{\mu}(\omega)$,

$$\hat{g}(\omega)=\frac{\hat{f}(\omega)}{\hat{\mu}(\omega)}, \quad (13)$$

Eq. (12) reduces to the form

$$\gamma_M(\mathbf{r})=\frac{2}{N}\int\int\Phi(\boldsymbol{\theta},\boldsymbol{\alpha})\int_0^\infty\hat{p}_s(\boldsymbol{\theta},\boldsymbol{\alpha},\omega)\times e^{-ik[R+(\boldsymbol{\alpha}-\boldsymbol{\theta})\cdot\mathbf{r}]}d\omega dS_\alpha dS_\theta. \quad (14)$$

The choice of frequency weight from Eq. (13) allows the multiple-frequency reconstruction formula of Eq. (12) to be greatly simplified. Specifically, the inner integral of Eq. (14) resembles a weighted inverse Fourier transform of the frequency-domain scattered field $\hat{p}(\boldsymbol{\theta},\alpha,\omega)$. To obtain an explicit time-domain expression for $\gamma_M(\mathbf{r})$, Eq. (14) can be rewritten using the definition of $\hat{p}_s(\boldsymbol{\theta},\boldsymbol{\alpha},\omega)$ from Eq. (5) to yield

$$\gamma_M(\mathbf{r})=\frac{1}{N}\int\int\Phi(\boldsymbol{\theta},\boldsymbol{\alpha})\times\mathbf{L}\left[p_s\left(\boldsymbol{\theta},\boldsymbol{\alpha},R/c_0+\frac{(\boldsymbol{\alpha}-\boldsymbol{\theta})\cdot\mathbf{r}}{c_0}\right)\right]dS_\alpha dS_\theta, \quad (15)$$

where $\mathbf{L}$ denotes the linear operator

$$\mathbf{L}[\psi(t)]=2\int_0^\infty\hat{\psi}(\omega)e^{-i\omega t}d\omega \quad (16)$$

and $\hat{\psi}(\omega)$ is the Fourier transform of $\psi(t)$ using the definition from Eq. (5).

Using the conjugate symmetry of $\hat{\psi}(\omega)$ [i.e., $\hat{\psi}(\boldsymbol{\theta},\boldsymbol{\alpha},\omega)=\hat{\psi}^*(\boldsymbol{\theta},\boldsymbol{\alpha},-\omega)$ for any real $\psi(t)$], the real part of

$\mathbf{L}[\psi(t)]$ is shown to be simply $\psi(t)$. Similarly, using the convolution theorem as well as the conjugate symmetry of $\psi(t)$, the imaginary part of $\mathbf{L}[\psi(t)]$ is seen to be an inverse Hilbert transform[28] of $\psi(t)$,

$$\mathrm{Im}[\mathbf{L}[\psi(t)]] = -\frac{1}{\pi}\int_{-\infty}^{\infty}\frac{\psi(\tau)}{t-\tau}\,d\tau = \mathbf{H}^{-1}[\psi(t)]. \quad (17)$$

This transform, also known as a quadrature filter, applies a phase shift of $\pi/2$ to each frequency component of the input signal.

Thus, the time-domain reconstruction formula can finally be written

$$\gamma_M(\mathbf{r}) = \frac{1}{N}\int\int \Phi(\boldsymbol{\theta},\boldsymbol{\alpha})\Big(p_s(\boldsymbol{\theta},\alpha,\tau) + i\mathbf{H}^{-1}[p_s(\boldsymbol{\theta},\alpha,\tau)]\Big)\,dS_\alpha dS_\theta, \quad (18)$$

where

$$\tau = R/c_0 + \frac{(\boldsymbol{\alpha}-\boldsymbol{\theta})\cdot\mathbf{r}}{c_0}. \quad (19)$$

The direction-dependent weight $\Phi(\boldsymbol{\theta},\boldsymbol{\alpha})$, which is the same as the ''filter'' employed in single-frequency filtered backpropagation, is given for the 2D and 3D cases by Eq. (9).

Equation (18) is notable in several respects. First, it provides a linearized reconstruction that employs scattering information from the entire signal bandwidth without any frequency decomposition of the scattered wavefield. Second, the delay term τ corresponds exactly to the delay required to construct a focus at the point $\mathbf{r}$ by delaying and summing the scattered wavefield $p_s(\boldsymbol{\theta},\boldsymbol{\alpha},t)$ for all measurement directions $\boldsymbol{\theta}$ and incident-wave directions $\boldsymbol{\alpha}$. Thus, the time-domain reconstruction formula given by Eq. (18) can be regarded as a quantitative generalization of confocal time-domain synthetic aperture imaging, in which signals are synthetically delayed and summed for each transmit/receive pair to focus at the image point of interest.[22,29,30]

A reconstruction formula similar to, although less general than, Eq. (18) was independently derived in Ref. 23 for the two-dimensional inverse scattering problem. In view of the present derivation, the method of ''probing by plane pulses'' in Ref. 23 can be regarded to yield a multiple-frequency reconstruction of $\mathrm{Re}[\gamma_M(\mathbf{r})]$, while the present method yields the complex function $\gamma_M(\mathbf{r})$. In Ref. 23, this method was proposed as a more convenient way to implement narrow-band diffraction tomography. However, the numerical results given below show that the reconstruction formula of Eq. (18), when directly implemented using wideband signals, provides considerable improvement in image quality over narrow-band reconstructions.

Reconstructions using Eq. (18) can be performed using any pulse waveform. However, the frequency compounding defined by Eq. (10) is most straightforwardly interpreted if the frequency weight $\hat{g}(\omega)$ has a phase that is independent of frequency. This criterion can be met, for instance, if the incident pulse waveform $f(t)$ is even in time,

$$f(t) = f(-t), \quad (20)$$

so that $\hat{f}(\omega)$ is purely real. [Similarly, if the incident pulse waveform is odd in time, $\hat{f}(\omega)$ is purely imaginary and Eq. (18) can still be employed.]

However, supposition of a frequency-independent phase for $\hat{f}(\omega)$ does not result in any loss of generality. For any linear-phase signal, such that the Fourier transform has the form

$$\hat{f}(\omega) = |\hat{f}(\omega)|e^{i\omega\zeta}, \quad \omega > 0, \quad (21)$$

an additional delay term of magnitude ζ can be applied to all scattered signals to obtain the signals associated with the purely-real spectrum $|\hat{f}(\omega)|$. In general, the scattered field associated with a desired waveform $f(t)$ can be determined for an arbitrary waveform $u(t)$ from the deconvolution operation

$$[p_s(\boldsymbol{\theta},\boldsymbol{\alpha},t)]_{f(t)} = \mathbf{F}^{-1}\left[\frac{\hat{f}(\omega)}{\hat{u}(\omega)}[p_s(\boldsymbol{\theta},\boldsymbol{\alpha},t)]_{u(t)}\right]. \quad (22)$$

For stable deconvolution using Eq. (22), the desired $\hat{f}(\omega)$ should not have significant frequency components outside the bandwidth of $\hat{u}(\omega)$.

B. Extensions to the reconstruction algorithm

For large tissue structures at high ultrasonic frequencies, weak scattering approximations such as the Born approximation are of limited validity. Thus, for problems of interest to medical ultrasonic imaging, reconstructed image quality can be improved by aberration correction methods that incorporate higher-order scattering and propagation effects. The present time-domain reconstruction formula (18) provides a natural framework for quantitative imaging with aberration correction. In general, if the background medium is known or can be estimated, the received scattered signals can be processed to provide an estimate of the scattered field that would be measured for the same scatterer within a homogeneous background medium. This approach essentially removes higher-order scattering effects from the measured far field scattering, so that a Born inversion can be performed on the modified data; similar processes occur implicitly in many nonlinear inverse scattering methods.[31]

For example, a simple implementation of aberration correction can be derived if one makes the assumption that background inhomogeneities result only in cumulative delays (or advances) of the incident and scattered wavefronts. This crude model does not include many propagation and scattering effects important to ultrasonic aberration, but has been shown to provide a reasonable first approximation of local delays in wavefronts propagating through large-scale tissue models.[32,33] Given this approximation, the total delay for an angle ϕ and a point position $\mathbf{r}$ is given by

$$\delta\tau(\boldsymbol{\phi},\mathbf{r}) = \int_{\xi} c(\boldsymbol{\xi})^{-1}d\xi - \frac{R}{c_0}, \quad (23)$$

where the integral is performed along the line that joins the spatial points $\mathbf{r}$ and $R\boldsymbol{\phi}$, Aberration-corrected reconstructions can then be performed using Eq. (18) with τ replaced by the corrected delay term

$$\tau \rightarrow R/c_0 + \frac{(\boldsymbol{\alpha}-\boldsymbol{\theta})\cdot\mathbf{r}}{c_0} + \delta\tau(\boldsymbol{\alpha},\mathbf{r}) + \delta\tau(\boldsymbol{\theta},\mathbf{r}). \tag{24}$$

Improved approximations could be obtained by application of the delay function $\delta\tau(\boldsymbol{\phi},\mathbf{r})$ after numerical backpropagation of the far-field scattered wavefronts through a homogeneous medium[34,35] or by compensation for both delay and amplitude variations.[36,37] More general, although much more computationally expensive, aberration correction could also be performed by synthetic focusing using full-wave numerical computation of acoustic fields within an estimated realization of the unknown medium. A method of this kind has been implemented, within the context of a frequency-domain diffraction tomography method, in Ref. 19.

The present imaging method has been derived using simplifying assumptions including zero absorption and constant density for the scattering medium. However, these assumptions do not substantially restrict the validity of the method. For example, the effect of absorption can be reduced using time-gain compensation, with or without frequency-dependent corrections,[38] of received scattered signals for each transmit/receive pair. Such time-gain compensation could be performed either using an estimated bulk attenuation for the medium (as with current clinical ultrasound scanners), or by implementation of an adaptive attenuation model in a manner similar to the time-shift compensation scheme discussed above.

Inclusion of density variations as well as sound speed variations adds additional complication to the time-domain diffraction tomography algorithm derived here. For single-frequency diffraction tomography in the presence of sound speed and density variations, the quantity $\gamma_B(\mathbf{r},\omega)$ reconstructed by Eq. (8) can be shown[39] to provide an estimate of a physical quantity that depends both on sound speed variations and density variations. In the notation used here, this quantity can be written

$$\gamma'(\mathbf{r}) = \gamma(\mathbf{r}) - \gamma(\mathbf{r})\,\gamma_\rho(\mathbf{r}) + \frac{1}{2k^2}\,\nabla^2\gamma_\rho(\mathbf{r}), \tag{25}$$

where the density variation is defined $\gamma_\rho = 1-\rho_0/\rho(\mathbf{r})$. Thus, for time-domain reconstructions of media with density variations, the reconstruction formula of Eq. (18) will provide the estimate

$$\gamma_M(\mathbf{r}) \approx \gamma(\mathbf{r}) - \gamma(\mathbf{r})\,\gamma_\rho(\mathbf{r}) + \frac{1}{2k_0^2}\,\nabla^2\gamma_\rho(\mathbf{r}), \tag{26}$$

where k_0 is the wave number corresponding to the center frequency of the pulse employed. For media such as human tissue, where density variations are fairly small and abrupt density transitions are rare, the last two terms of Eq. (26) are small compared to $\gamma(\mathbf{r})$, so that the reconstruction algorithm derived above can still be regarded to provide an image of the sound-speed variation function $\gamma(\mathbf{r})$. However, if desired, a reconstruction employing pulses with two distinct center frequencies could allow separation of sound speed and density variations by techniques similar to those described in Ref. 16 or 39.

II. COMPUTATIONAL METHODS

The time-domain inverse scattering method described above has been tested with 2D and 3D synthetic data prepared using three numerical methods: a Born approximation method for point scatterers and 3D slabs, an exact series solution for cylindrical inhomogeneities, and a *k*-space method for arbitrary 2D inhomogeneous media.

The time-domain waveform employed for all the computations reported here was

$$f(t) = \cos(\omega_0 t)\,e^{-t^2/(2\sigma^2)}, \tag{27}$$

where $\omega_0 = 2\pi f_0$ for a center frequency of f_0 and σ is the temporal Gaussian parameter. This waveform has the real, even Fourier transform

$$\hat{f}(\omega) = \sqrt{\frac{\sigma^2}{8\pi}}\left(e^{-\sigma^2(\omega-\omega_0)^2/2} + e^{-\sigma^2(\omega+\omega_0)^2/2}\right). \tag{28}$$

Values used for the computations reported here were $f_0 = 2.5$ MHz and $\sigma = 0.25$ μs, so that the -6 dB bandwidth of the signal was 1.5 MHz. These parameters correspond closely to those of an existing 2048-element ring transducer.[40]

For the case of point scatterers, the contrast function γ was assumed to take the form

$$\gamma(\mathbf{r}) = \sum_1^M \mu_j\,\delta(\mathbf{r}-\mathbf{r_j}). \tag{29}$$

Using the far-field form of the 2D Green's function and neglecting multiple scattering, Eq. (6) for the scattered far field can be rewritten as

$$\hat{p}_s(\boldsymbol{\theta},\boldsymbol{\alpha},\omega) = -k^2\sqrt{\frac{i}{8\pi kR}}\,\hat{f}(\omega)\sum_j \mu_j e^{ik(\boldsymbol{\alpha}-\boldsymbol{\theta})\cdot\mathbf{r}_j} \tag{30}$$

for each frequency component of interest. Time-domain waveforms were synthesized by using Eq. (30) for each frequency with $\hat{f}(\omega) > 10^{-3}$ and inverting the frequency-domain scattered wavefield by a fast Fourier transform (FFT) implementation of Eq. (4). The temporal sampling rate employed was 10 MHz. An analogous formula, with a different multiplicative constant, was also employed for the 3D case.

The Born approximation was also used to compute three-dimensional scattering for slab-shaped objects defined by the equation

$$\gamma(\mathbf{r}) = \gamma_0 H(a_x - |x|)H(a_y - |y|)H(a_z - |z|). \tag{31}$$

For this object, the linearized forward problem can be solved analytically. Under the Born approximation, the frequency-domain scattered far field has the form

$$\begin{aligned}\hat{p}_s(\boldsymbol{\theta},\boldsymbol{\alpha},\omega) = {} & 2\hat{f}(\omega)\,\gamma_0 a_x a_y a_z e^{ikR}/(\pi R) \\ & \times \frac{\sin[kL_x(\boldsymbol{\alpha}-\boldsymbol{\theta})\cdot\mathbf{e}_x]}{kL_x(\boldsymbol{\alpha}-\boldsymbol{\theta})\cdot\mathbf{e}_x}\,\frac{\sin[kL_y(\boldsymbol{\alpha}-\boldsymbol{\theta})\cdot\mathbf{e}_y]}{kL_y(\boldsymbol{\alpha}-\boldsymbol{\theta})\cdot\mathbf{e}_y} \\ & \times \frac{\sin[kL_z(\boldsymbol{\alpha}-\boldsymbol{\theta})\cdot\mathbf{e}_z]}{kL_z(\boldsymbol{\alpha}-\boldsymbol{\theta})\cdot\mathbf{e}_z},\end{aligned} \tag{32}$$

where $\mathbf{e}_x$, $\mathbf{e}_y$, and $\mathbf{e}_z$ represent unit vectors in the *x*, *y*, and *z* directions. The time domain scattered pressure $p_s(\boldsymbol{\theta},\boldsymbol{\alpha},t)$ is

obtained, as for the point scatterer case described above, by inverse transformation of the frequency-domain wavefield for all frequencies within the bandwidth of interest.

For 2D cylindrical inhomogeneities, an analogous procedure was followed, except that the frequency-domain scattered wavefield $\hat{p}_s(\boldsymbol{\theta},\boldsymbol{\alpha},\omega)$ was computed using an exact series solution[25] for each frequency component of interest. In implementation of the series solution, summations were truncated when the magnitude of a single coefficient dropped below 10^{-12} times the sum of all coefficients.

Solutions were also obtained for arbitrary 2D inhomogeneous media using a time-domain *k*-space method.[41] Grid sizes of 256×256 points, a spatial step of 0.0833 mm, and a time step of 0.02734 μs were employed. Scattered acoustic pressure signals on a circle of virtual receivers were recorded at a sampling rate of 9.144 MHz. The receiver circle, which had a radius of 3.0 mm in these computations, completely contained the inhomogeneities used. Far-field waveforms were computed by Fourier transforming the time-domain waveforms on the near-field measurement circle, transforming these to far-field waveforms for each frequency using a numerically exact transformation method,[16] and performing inverse Fourier transformation to yield time-domain far-field waveforms. All forward and inverse temporal Fourier transforms, as well as angular transforms occurring in the near-field-far-field transformation,[16] were performed by FFT.

The time-domain imaging method was directly implemented using Eq. (18), evaluated using straightforward numerical integration over all incident-wave and measurement directions employed. The reconstruction formula employed can be explicitly written as

$$\gamma_M(\mathbf{r})=\frac{1}{N_{2D}}\int_0^{2\pi}\int_0^{2\pi}|\sin(\alpha-\theta)|\Big(p_s(\boldsymbol{\theta},\boldsymbol{\alpha},\tau)+i\mathbf{H}^{-1}[p_s(\boldsymbol{\theta},\boldsymbol{\alpha},\tau)]\Big)\,d\alpha\,d\theta,$$
$$\tau=R/c_0+\frac{(\cos\alpha-\cos\theta)\cdot x+(\sin\alpha-\sin\theta)\cdot y}{c_0} \tag{33}$$

for the 2D case, where α and θ are the angles corresponding to the direction vectors $\boldsymbol{\alpha}$ and $\boldsymbol{\theta}$, and as

$$\gamma_M(\mathbf{r})=\frac{1}{N_{3D}}\int_0^{2\pi}\int_0^{\pi}\int_0^{2\pi}\int_0^{\pi}|\boldsymbol{\alpha}-\boldsymbol{\theta}|\Big(p_s(\boldsymbol{\theta},\boldsymbol{\alpha},\tau)+i\mathbf{H}^{-1}[p_s(\boldsymbol{\theta},\boldsymbol{\alpha},\tau)]\Big)\sin(\Phi_{\boldsymbol{\alpha}})\sin(\Phi_{\theta})\,d\Phi_{\boldsymbol{\alpha}}\times d\Theta_{\boldsymbol{\alpha}}d\Phi_{\boldsymbol{\theta}}d\Theta_{\boldsymbol{\theta}},$$
$$\tau=R/c_0+\frac{(\boldsymbol{\alpha}-\boldsymbol{\theta})\cdot\mathbf{r}}{c_0}, \tag{34}$$
$$\boldsymbol{\alpha}-\boldsymbol{\theta}=(\cos\Theta_{\boldsymbol{\alpha}}\sin\Phi_{\boldsymbol{\alpha}}-\cos\Theta_{\boldsymbol{\theta}}\sin\Phi_{\boldsymbol{\theta}})\cdot\mathbf{e}_x+(\sin\Theta_{\boldsymbol{\alpha}}\sin\Phi_{\boldsymbol{\alpha}}-\sin\Theta_{\boldsymbol{\theta}}\sin\Phi_{\boldsymbol{\theta}})\cdot\mathbf{e}_y+(\cos\Phi_{\boldsymbol{\alpha}}-\cos\Phi_{\boldsymbol{\theta}})\cdot\mathbf{e}_z$$

for the 3D case, where $\Theta_{\boldsymbol{\alpha}}$ and $\Phi_{\boldsymbol{\alpha}}$ are direction angles for the incident-wave direction $\boldsymbol{\alpha}$ and $\Theta_{\boldsymbol{\theta}}$ and $\Phi_{\boldsymbol{\theta}}$ are direction angles for the measurement direction $\boldsymbol{\theta}$. For each case, the normalization factor N was determined from Eq. (11) with $\hat{g}(\omega)=\hat{f}(\omega)/\hat{\mu}(\omega)$ and $\mu(\omega)$ given by Eq. (9). Before evaluation of the argument τ for each signal, the time-domain waveforms were resampled at a sampling rate of 16 times the original rate. This resampling was performed using FFT-based Fourier interpolation. The inverse Hilbert transform was performed for each signal using an FFT implementation of Eq. (16). Values of the pressure signals at the time τ were then determined using linear interpolation between samples of the resampled waveforms. The integrals of Eqs. (33) and (34) were implemented using discrete summation over all transmission and measurement directions employed.

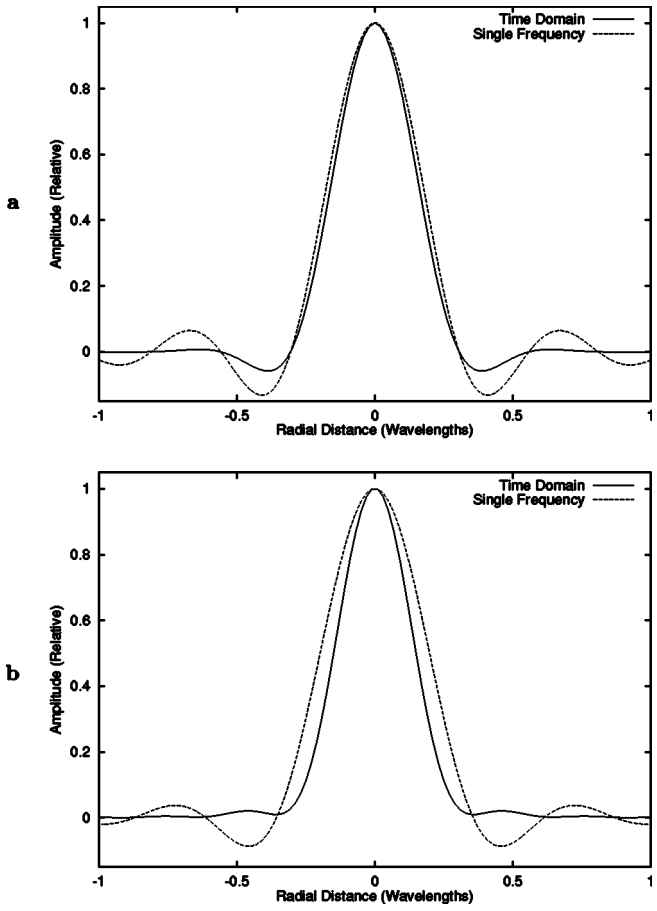

FIG. 2. Point-spread functions for time-domain and single-frequency diffraction tomography methods. In each panel, the vertical scale corresponds to the relative amplitude of the reconstructed contrast $\gamma(\mathbf{r})$, while the horizontal scale corresponds to number of wavelengths at the center frequency. (a) Two-dimensional case. (b) Three-dimensional case.

Computations were also performed using the time-domain diffraction tomography algorithm for limited-aperture data. For these reconstructions, the integrals of Eq. (33) were evaluated only for angles corresponding to transmitters and receivers within a specified aperture of angular width ϕ_{ap}, i.e.,

$$|\alpha|\leq\phi_{\mathrm{ap}}/2,\quad|\theta-\pi|\leq\phi_{\mathrm{ap}}/2. \tag{35}$$

Use of a small value for ϕ_{ap} corresponds to use of a small aperture in pulse-echo mode.

III. NUMERICAL RESULTS

Two-dimensional and three-dimensional point-spread functions (PSF) for the present time-domain diffraction tomography method are illustrated in Fig. 2. The time-domain reconstructions shown here, like the other time-domain reconstructions shown in this paper, were obtained using a incident pulse of center frequency 2.5 MHz and a Gaussian envelope corresponding to a -6 dB bandwidth of 1.5 MHz. Point-spread functions were determined by reconstructing a point scatterer located at the origin. For the 2D case, in which the point scatterer can be regarded as a thin wire, synthetic scattering data was obtained using the Born approximation method outlined above for 16 incident-wave directions and 64 measurement directions. The 3D time-domain reconstruction was obtained using Born data for 72 incident-wave directions and 288 measurement directions, each evenly spaced on a rectangular grid defined by the angles Θ and Φ. For comparison, analogous point-spread functions are also shown for standard frequency-domain diffraction tomography reconstructions using single-frequency (2.5 MHz) data.

For the 2D case illustrated in Fig. 2, the time-domain PSF has a slightly narrower peak, indicating that point resolution has been slightly improved by the increased bandwidth employed in the time domain method. More significantly, sidelobes of the time-domain PSF are significantly smaller than those for the single-frequency PSF (the first sidelobe is reduced by 7 dB, while the second is reduced by 19 dB), so that contrast resolution for time-domain diffraction tomography is seen to be much higher than for single-frequency diffraction tomography. For the 3D case, the time-domain reconstruction shows a much more dramatic improvement over the single-frequency reconstruction. In this case, the time-domain solution shows significant increases in both the point resolution (PSF width at half-maximum reduced by 27%) and contrast resolution (first sidelobe reduced by 13 dB and second sidelobe reduced by 18 dB). Furthermore, a comparison of the PSFs for 2D and 3D time-domain reconstruction indicates that much higher image quality is achievable for 3D time-domain imaging than for the 2D case. This increase in image quality suggests that the time-domain diffraction tomography method proposed here may benefit from the overdetermined nature of the general wideband 3D inverse scattering problem.[42,43]

The effect of transmit and receive aperture characteristics on image quality is illustrated in Fig. 3. Panels (a) and (b) of Fig. 3 show the point-spread function for a number of aperture configurations, each employing 64 measurement directions. Figure 3(a) shows the point-spread function for reconstructions obtained using 1, 4, 8, and 16 incident-wave directions. The point scatterer is clearly imaged even for the reconstruction using one incident-wave direction. Optimal image quality (indistinguishable from reconstructions with 64 incident-wave directions) is obtained for 16 incident-wave directions, so that scattering data obtained using one incident-wave direction for each group of four measurement directions appears to be sufficient for the present reconstruction method.

The effect of limited view range on the point spread function is also illustrated in Fig. 3. Panel (b) shows the point-spread function for four differently limited apertures, while panel (c) shows reconstructions of a homogeneous cylinder ($a=1.0$ mm, $\gamma=0.02$) for the same apertures. In each case, limitation of the transmit and receive apertures to angles near the backscatter direction (aperture size $\pi/2$) results in images that resemble a conventional B-scans. Use of apertures corresponding to pulse-echo mode in the large-aperture limit (aperture size π) yield higher resolution in all directions. Using three-fourths of a circular aperture (size $3\pi/2$) yields image quality close to that for the full aperture (2π) case. The characteristics of all these images result from the set of spatial-frequency vectors interrogated by each group of scattering measurements.[1] Apertures with only a limited range of transmit and receive directions [e.g., the ''b-scan'' apertures shown in the first column of panels (b) and (c)] provide only information corresponding to large spatial frequency vectors oriented nearly on-axis, so that such images mainly show those edges that are nearly perpendicular to the axis of the aperture.

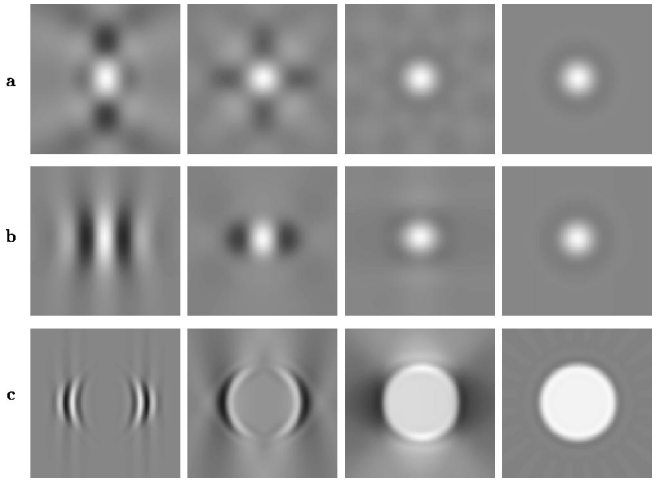

FIG. 3. Effect of aperture characteristics on image quality. Each panel shows the real part of a time-domain reconstruction, $\mathrm{Re}[\gamma_M]$, on a linear grayscale with white representing the maximum amplitude of $|\gamma_M(\mathbf{r})|$ and black represents -1 times the maximum amplitude. (a) Point-spread functions for the same waveform parameters as Fig. 2. Each panel shows an area of 0.6×0.6 mm^2, corresponding to one square wavelength at the center frequency. Left to right: 1, 4, 8, and 16 incident-wave directions. (b) Point-spread functions for aperture sizes of $\pi/2$, π, $3\pi/2$, and 2π radians, format as in previous panel. (c) Real parts of reconstructions for a homogeneous cylinder ($a=1.0$ mm, $\gamma=0.02$). The area shown in each panel is 2.0×2.0 mm^2.Left to right: aperture sizes of $\pi/2$, π, $3\pi/2$, and 2π radians.

Reconstructions performed using exact solutions for scattering from cylindrical inhomogeneities provide a straightforward means to assess the accuracy of the time-domain scattering method for a range of object sizes and contrasts. A number of example reconstructions are shown in Figs. 4 and 5. The number of measurement directions for all cylinder reconstructions was chosen based on an empirical test of the number required for a satisfactory image of a homogeneous cylinder; for a cylinder of radius 1 mm, the required number of measurement directions was determined to be approximately 96. Based on spatial-frequency sampling considerations, the number of measurement directions was increased in proportion to the size of the inhomogeneous

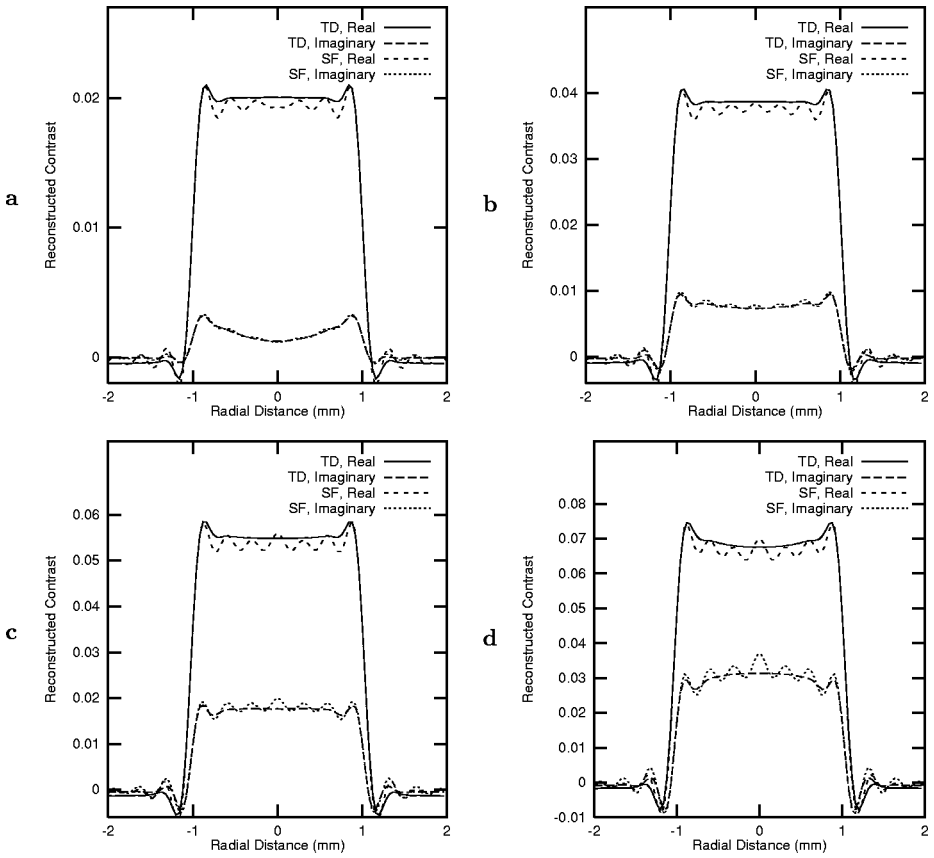

FIG. 4. Cross sections of reconstructed contrast functions $\gamma(\mathbf{r})$ for a cylinder of radius 1 mm, using time-domain (TD) and single-frequency (SF) diffraction tomography. Waveform parameters are as in Fig. 1. (a) $\gamma=0.02$. (b) $\gamma=0.04$. (c) $\gamma=0.06$. (d) $\gamma=0.08$.

region to be reconstructed. Since the results shown in Fig. 3 indicate that considerably fewer incident-wave directions than measurement directions are needed, the number of incident directions was chosen to be one-quarter the number of measurement directions in each case.

Cross sections of time-domain and single-frequency reconstructions, plotted in Fig. 4, show the relative accuracy of each reconstruction method for a cylinder of 1-mm radius and purely real contrast ranging from $\gamma=0.02$ to $\gamma=0.08$. For the synthetic scattering data in each case, 96 measurement directions and 24 incident-wave directions were employed. The time-domain reconstructions show improvement over the single-frequency reconstructions both in improved contrast resolution (smaller sidelobes outside the support of the cylinder) and in decreased ringing (Gibbs phenomenon) artifacts within the support of the cylinder. However, for increasing contrast values, both methods show similar increases in phase error, as indicated by increased imaginary parts of the reconstructed contrast. This error results from the Born approximation, which is based on the assumption that the incident wave propagates through the inhomogeneous medium without distortion. Perturbations in the local arrival time of the incident wavefront, which are more severe for higher contrasts and larger inhomogeneities, can result in a scattered field that is phase shifted relative to the ideal case assumed in the Born approximation; linear inversion of this phase-distorted data naturally results in a phase-distorted reconstruction of the scattering medium. (A complementary explanation of this phase error, based on the unitarity of the scattering operator, is given in Ref. 19.)

A test of image fidelity for the time-domain reconstruction method is shown in Fig. 5. The real parts of time-domain reconstructions are shown as grayscale images for homogeneous cylinders with radii between 1 and 4 mm and contrasts between $\gamma=0.02$ and $\gamma=0.08$. The number of measurement directions employed for the synthetic scattering data was 96 for the 1-mm radius cylinders, 192 for the 2-mm cylinders, 288 for the 3-mm cylinders, and 384 for the 4-mm cylinders. In each case, four incident-wave directions per measurement direction were used. The first row of this figure corresponds to the time-domain reconstructions shown in Fig. 4.

The images shown in Fig. 5 provide a basis for evaluating the ability of the present time-domain diffraction tomography method to image homogeneous objects of various sizes and contrasts. In this figure, images of $\mathrm{Re}[\gamma_M]$ show uniform quality for small cylinder sizes and contrasts, but poorer image quality for larger sizes and contrasts. For the largest size and contrast employed ($a=4.0$ mm, $\gamma=0.08$), the reconstruction primarily shows the edges of the cylinder and fails to image the interior. Particularly notable is that the ''matrix'' of images in Fig. 5 is nearly diagonal; that is, a linear increase in object contrast causes image degradation comparable to a corresponding linear increase in object size. Thus, a nondimensional parameter directly relevant to image quality for homogeneous objects is $ka\,\gamma$, where k is a domi-

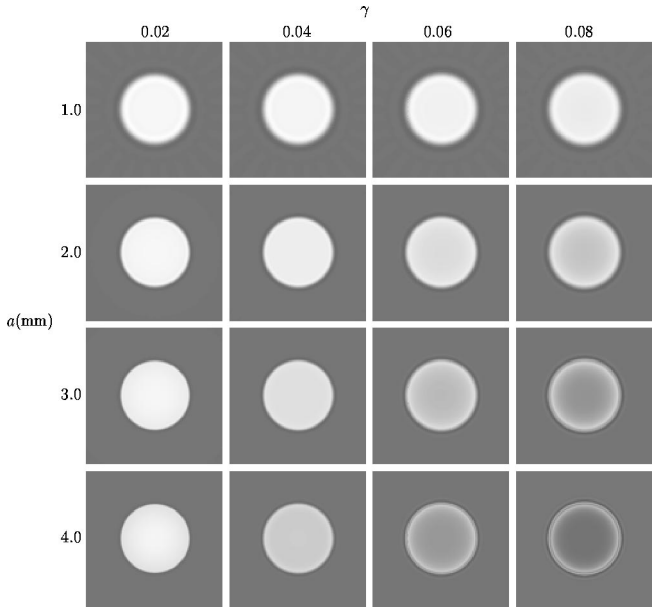

FIG. 5. Images of time-domain reconstructions for cylinders of varying radius a and contrast γ. Each panel shows the real part of the reconstructed contrast, $\mathrm{Re}[\gamma_M(\mathbf{r})]$, for a pulse of center frequency 2.5 MHz and -6 dB bandwidth 1.5 MHz. The area shown in each panel is $2a\times 2a$. All images are shown on a linear, bipolar gray scale where white represents the maximum amplitude of $|\gamma_M(\mathbf{r})|$ and black represents -1 times the maximum amplitude.

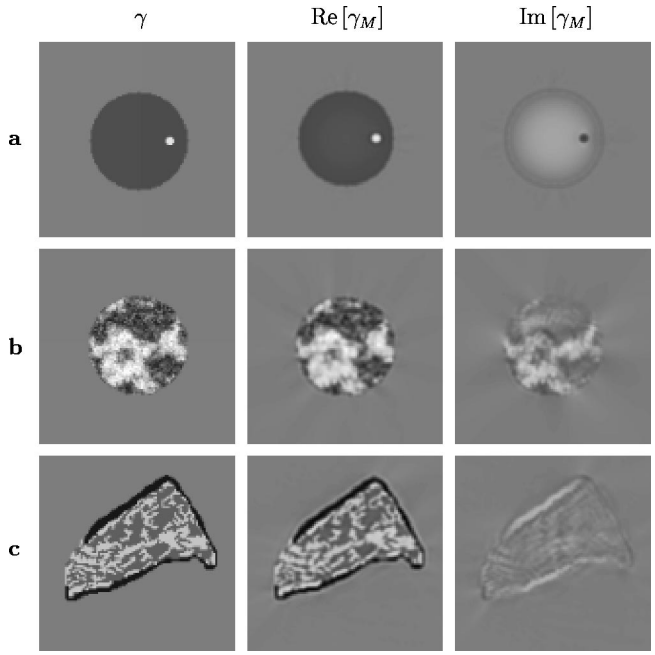

FIG. 6. Time-domain reconstructions from full-wave synthetic data for three arbitrary scattering objects. Each row shows the actual (purely real) contrast function γ together with the real and imaginary parts of the reconstructed contrast function γ_M, using the same linear bipolar gray scale for each panel. Each panel shows a reconstruction area of 5×5 mm^2. (a) Cylinder, radius 2.5 mm, with an internal cylinder of radius 0.2 mm. (b) Cylinder, radius 2.5 mm, with random internal structure. (c) Tissue structure, with variable sound speed and density, from chest wall cross section 5L in Ref. 45.

nant wave number, a is the object radius, and γ is the object contrast. Using the wave number $k_0=10.472$ rad/mm corresponding to the center frequency of 2.5 MHz and a sound speed of 1.5 mm/μs, the reconstructions shown in Fig. 5 indicate that the interior of the cylinder is imaged satisfactorily for the approximate range $ka\ \gamma<2.5$. This result is consistent with a previous study of single-frequency diffraction tomography, in which adequate Born reconstructions of cylinders were obtained for the parameter range $ka\ \gamma\leqslant 2.2$.[44]

Reconstructions for several scattering objects without special symmetry are shown in Fig. 6. All of these reconstructions were performed using synthetic data produced by the k-space method described in Ref. 41. Synthetic scattering data were computed for 64 incident-wave directions and 256 measurement directions in each case. The first panel shows a reconstruction of a cylinder of radius 2.5 mm and contrast $\gamma=-0.0295$ with an internal cylinder of radius 0.2 mm and contrast $\gamma=0.0632$. These contrast values correspond, based on tissue parameters given in Ref. 32, to the sound-speed contrasts of human skeletal muscle for the outer cylinder and of human fat for the inner cylinder. The second panel shows a reconstruction of a 2.5-mm-radius cylinder with random internal structure. The third reconstruction shown employed a portion of a chest wall tissue map from Ref. 45. In this case, the synthetic data was obtained using a tissue model[45] that incorporates both sound speed and density variations, so that the reconstructed quantity is given by Eq. (26). In Fig. 6(c), black denotes connective tissue ($\gamma=-0.1073$, $\gamma_\rho=0.1134$), dark gray denotes muscle ($\gamma=-0.0295$, $\gamma_\rho=0.0543$), and light gray denotes fat ($\gamma=0.0632$, $\gamma_\rho=-0.0453$).

The real part of each reconstruction in Fig. 6 shows good image quality, with high resolution and very little evidence of artifacts. Particularly notable is the accurately detailed imaging of internal structure for the random cylinder and the chest wall cross section. As expected, the density variations present in the chest wall cross section have not greatly affected the image appearance; there is, however, a slight edge enhancement, associated with the Laplacian term in Eq. (26), at boundaries between tissue regions. Also notable is the nearly complete absence of any artifacts outside the scatterer in each case; this result indicates that high contrast resolution has been achieved. However, in each case, the imaginary part of the reconstruction is nonzero, indicating that the Born approximation is not fully applicable. The imaginary parts of each reconstruction are, however, small compared to the real parts. Thus, simple aberration correction methods [of which one example is given by Eq. (24)] could substantially reduce this phase error, as for multiple-frequency diffraction tomography in Ref. 19.

Three-dimensional reconstructions of a homogeneous slab are shown in Fig. 7. The scatterer is characterized by Eq. (31) with $\gamma_0=0.01$, $a_x=0.5$ mm, $a_y=1.0$ mm, and $a_z=1.5$ mm. Synthetic data was computed using Eq. (34) for 288 incident-wave directions and 1152 measurement directions, each evenly spaced in the angles Φ and Θ. Signal parameters were as for the examples above, except that the initial sampling rate for the time-domain signals was 9.0 MHz. Isosurface renderings of the real part of γ_M are shown for the surfaces $\gamma_M=0.0025$. Since the scattering data were obtained using a Born approximation for the 3D case, the

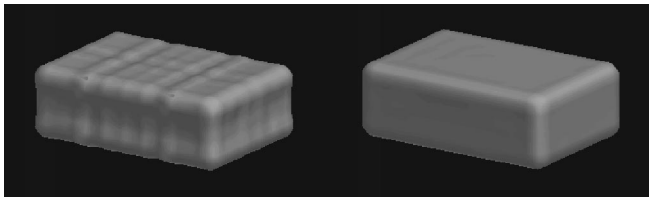

FIG. 7. Three-dimensional reconstructions of a uniform slab with contrast $\gamma = 0.01$. Each reconstruction shows an isosurface rendering of the surface $\gamma_M = 0.0025$. Left: single-frequency reconstruction. Right: time-domain reconstruction.

imaginary part of each reconstruction is identically zero for both reconstructions. Consistent with the point-spread functions shown in Fig. 2, the time-domain reconstruction is much more accurate than the single-frequency reconstruction. While the single-frequency reconstruction shows an erroneously rippled surface, the time-domain reconstruction is smooth. The time-domain reconstruction is nearly identical to the original object except for some rounding of the sharp edges due to the limited high-frequency content of the signal employed. The length scale of the rounded edges is on the order of one-half the wavelength of the highest frequency in the pulse, i.e., about 0.2 mm for the -6-dB cutoff of 3.25 MHz.

Since three-dimensional inverse scattering is a computationally demanding problem, comparison of computational efficiency for single-frequency and time-domain methods is of interest. For both reconstructions shown in Fig. 7, identical discretizations of the reconstructed medium were employed. Both computations included solution of the applicable linearized forward problem as well as the inverse problem. Nonetheless, the time-domain method was more efficient than the single-frequency method; the total CPU time required on a 200-MHz AMD K6 processor was 133.3 CPU min for the time-domain method and 287.4 CPU min for the single-frequency method. This gain in efficiency was possible because the greatest computational expense occurred in the ''backpropagation'' of the signals for each reconstruction point. For the single-frequency method, this step required evaluation of complex exponentials for each incident-wave direction, measurement direction, and spatial point. For the time-domain method, however, the computationally intensive steps (including the forward problem solution and Fourier interpolation of the scattered signals) needed only to be performed once for each transmit/receive pair. For the backpropagation step, performed at each point in the 3D spatial grid, the time-domain reconstruction method required only linear interpolation of the oversampled farfield pressure waveforms.

IV. CONCLUSIONS

A new method for time-domain ultrasound diffraction tomography has been presented. The method provides quantitative images of sound speed variations in unknown media; when two pulse center frequencies are employed, the method is also capable of imaging density variations. Reconstructions performed using this method are equivalent to multiple-frequency reconstructions using filtered backpropagation, but can be obtained with much greater efficiency.

The time-domain reconstruction algorithm has been derived as a simple filtered delay-and-sum operation applied to far-field scattered signals. This algorithm is closely related to time-domain confocal synthetic aperture imaging, so that it can be considered a generalization of imaging algorithms employed in current clinical instruments. The simplicity of the imaging algorithm allows straightforward addition of features such as time-gain compensation and aberration correction.

Numerical results obtained using synthetic data for 2D and 3D scattering objects show that the time-domain method can yield significantly higher image quality (and, in some cases, also greater efficiency) than single-frequency diffraction tomography. Quantitative reconstructions, obtained using signal parameters comparable to those for present-day clinical instruments, show accurate imaging of objects with simple deterministic structure, random internal structure, and structure based on a cross-sectional tissue model. The method is hoped to be useful for diagnostic imaging problems such as the detection and characterization of lesions in ultrasonic mammography.

ACKNOWLEDGMENTS

This research was funded by the Breast Cancer Research Program of the U.S. Army Medical Research and Material Command, under Grant No. DAMD17-98-1-8141. The author is grateful for helpful discussions with Adrian I. Nachman, Feng Lin, and Robert C. Waag.

[1] E. Wolf, ''Three-dimensional structure determination of semi-transparent objects from holographic data,'' Opt. Commun. **1**, 153–156 (1969).
[2] A. J. Devaney, ''A filtered backpropagation algorithm for diffraction tomography,'' Ultrason. Imaging **4**, 336–350 (1982).
[3] D. T. Borup, S. A. Johnson, W. W. Kim, and M. J. Berggren, ''Nonperturbative diffraction tomography via Gauss-Newton iteration applied to the scattering integral equation,'' Ultrason. Imaging **14**, 69–85 (1992).
[4] S. Gutman and M. Klibanov, ''Two versions of quasi-Newton method for multidimensional inverse scattering problem,'' J. Comput. Acoust. **1**, 197–228 (1993).
[5] F. W. Kremkau, *Diagnostic Ultrasound: Physical Principles and Exercises* (Grune and Stratton, New York, 1980).
[6] J. L. Schwartz and B. D. Steinberg, ''Ultrasparse, ultrawideband arrays,'' IEEE Trans. Ultrason. Ferroelectr. Freq. Control **45**, 376–393 (1998).
[7] S. H. Maslak, ''Computed sonography,'' in *Ultrasound Annual 1985* (Raven, New York, 1985), pp. 1–16.
[8] E. L. Madsen, B. S. Garra, J. A. Parks, A. C. Skelly, and J. A. Zagzebski, *AIUM Quality Control Manual for Gray-Scale Ultrasound Scanners* (American Institute of Ultrasound in Medicine, Laurel, MD, 1995).
[9] S. J. Norton, ''Reconstruction of a two-dimensional reflecting medium over a circular domain: exact solution,'' J. Acoust. Soc. Am. **67**, 1266–1273 (1980).
[10] S. J. Norton and M. Linzer, ''Ultrasonic reflectivity imaging in three dimensions: exact inverse scattering solutions for plane, cylindrical, and circular apertures,'' IEEE Trans. Biomed. Eng. **28**, 202–220 (1980).
[11] J. H. Kim, S. B. Park, and S. A. Johnson, ''Tomographic imaging of ultrasonic reflectivity with correction for acoustic speed variations,'' Ultrason. Imaging **6**, 304–312 (1984).
[12] C. Q. Lan and W. Xiong, ''An iterative method of ultrasonic reflection mode tomography,'' IEEE Trans. Med. Imaging **13**, 419–425 (1994).
[13] D. Miller, M. Oristaglio, and G. Beylkin, ''A new slant on seismic imaging: migration and internal geometry,'' Geophysics **52**, 943–964 (1987).

[14] T. Melamed, Y. Ehrlich, and E. Heymann, ''Short-pulse inversion of inhomogeneous media: a time-domain diffraction tomography,'' Inverse Probl. **12**, 977–993 (1996).
[15] S. Pourjavid and O. Tretiak, ''Ultrasound imaging through time-domain diffraction tomography,'' IEEE Trans. Ultrason. Ferroelectr. Freq. Control **38**, 74–85 (1991).
[16] A. Witten, J. Tuggle, and R. C. Waag, ''A practical approach to ultrasonic imaging using diffraction tomography,'' J. Acoust. Soc. Am. **83**, 1645–1652 (1988).
[17] T. J. Cavicchi and W. D. O'Brien, ''Numerical study of higher-order diffraction tomography via the sinc basis moment method,'' Ultrason. Imaging **11**, 42–74 (1989).
[18] H. Gan, R. Ludwig, and P. L. Levin, ''Nonlinear diffractive inverse scattering for multiple scattering in inhomogeneous acoustic background media,'' J. Acoust. Soc. Am. **97**, 764–776 (1995).
[19] T. D. Mast, A. I. Nachman, and R. C. Waag, ''Focusing and imaging using eigenfunctions of the scattering operator,'' J. Acoust. Soc. Am. **102**, 715–725 (1997).
[20] J. M. Blackledge, R. E. Burge, K. I. Hopcraft, and R. J. Wombell, ''Quantitative diffraction tomography: I. Pulsed acoustic fields,'' J. Phys. D **20**, 1–10 (1987).
[21] S. Mensah and J.-P. Lefebvre, ''Enhanced compressibility tomography,'' IEEE Trans. Ultrason. Ferroelectr. Freq. Control **44**, 1245–1252 (1997).
[22] G. Prokoph and H. Ermert, ''A comparison of broadband holographic and tomographic imaging concepts,'' Acoust. Imaging **18**, 381–390 (1991).
[23] V. A. Burov and O. D. Rumyantseva, ''Linearized inverse problem of scattering in monochromatic and pulse modes,'' Acoust. Phys. **40**, 34–42 (1996).
[24] F. Lin, A. I. Nachman, and R. C. Waag, ''Quantitative imaging using a time-domain eigenfunction method,'' submitted to J. Acoust. Soc. Am. (1999).
[25] P. M. Morse and K. U. Ingard, *Theoretical Acoustics* (New York, McGraw-Hill, 1968), Chap. 8.
[26] P. M. Morse and H. Feshbach, *Methods of Theoretical Physics* (McGraw–Hill, New York, 1953), Vol. I.
[27] G. Beylkin, ''The fundamental identity for iterated spherical means and the inversion formula for diffraction tomography and inverse scattering,'' J. Math. Phys. **24**, 1399–1400 (1982).
[28] A. Papoulis, *The Fourier Integral and Its Applications* (McGraw–Hill, New York, 1962), Chap. 10.
[29] J. Ylitalo, E. Alasaarela, and J. Koivukangas, ''Ultrasound holographic B-scan imaging,'' IEEE Trans. Ultrason. Ferroelectr. Freq. Control **36**, 376–383 (1989).
[30] K. E. Thomenius, ''Evolution of ultrasound beamformers,'' Proc. IEEE Ultrason. Symp. **2**, 1615–1622 (1996).
[31] R. Snieder, ''A perturbative analysis of non-linear inversion,'' Geophys. J. Int. **101**, 545–556 (1990).
[32] T. D. Mast, L. M. Hinkelman, M. J. Orr, V. W. Sparrow, and R. C. Waag, ''Simulation of ultrasonic pulse propagation through the abdominal wall,'' J. Acoust. Soc. Am. **102**, 1177–1190 (1997) [Erratum: **104**, 1124–1125 (1998)].
[33] T. D. Mast, L. M. Hinkelman, M. J. Orr, and R. C. Waag, ''The effect of abdominal wall morphology on ultrasonic pulse distortion. Part II. Simulations,'' J. Acoust. Soc. Am. **104**, 3651–3664 (1998).
[34] D.-L. Liu and R. C. Waag, ''Correction of ultrasonic wavefront distortion using backpropagation and a reference waveform method for time-shift compensation,'' J. Acoust. Soc. Am. **96**, 649–660 (1994).
[35] C. Dorme and M. Fink, ''Ultrasonic beam steering through inhomogeneous layers with a time reversal mirror,'' IEEE Trans. Ultrason. Ferroelectr. Freq. Control **43**(1), 167–175 (1996).
[36] S. Kirshnan, P.-C. Li, and M. O'Donnell, ''Adaptive compensation for phase and magnitude aberrations,'' IEEE Trans. Ultrason. Ferroelectr. Freq. Control **43**(1), 44–55 (1996).
[37] Q. Zhu and B. D. Steinberg, ''Deabberation of incoherent wavefront distortion: an approach toward inverse filtering,'' IEEE Trans. Ultrason. Ferroelectr. Freq. Control **44**, 575–589 (1997).
[38] I. Claesson and G. Salomonsson, ''Frequency- and depth-dependent compensation of ultrasonic signals,'' IEEE Trans. Ultrason. Ferroelectr. Freq. Control **35**, 582–592 (1988).
[39] A. J. Devaney, ''Variable density acoustics tomography,'' J. Acoust. Soc. Am. **78**, 120–130 (1985).
[40] T. T. Jansson, T. D. Mast, and R. C. Waag, ''Measurements of differential scattering cross section using a ring transducer,'' J. Acoust. Soc. Am. **103**, 3169–3179 (1998).
[41] L. P. Souriau, T. D. Mast, D.-L. D. Liu, M.. Tabei, A. I. Nachman, and R. C. Waag, ''A *k*-space method for large-scale models of wave propagation in tissue,'' submitted to IEEE Trans. Ultrason. Ferrolectr. Freq. Control. (1999).
[42] A. Nachman, ''Reconstructions from boundary measurements,'' Ann. Math. **128**, 531–576 (1988).
[43] D. Colton and R. Kress, *Inverse Acoustic and Electromagnetic Scattering Theory*, 2nd ed. (Springer-Verlag, Berlin, 1998), Chap. 10.
[44] M. Slaney, A. C. Kak, and L. E. Larsen, ''Limitations of imaging with first-order diffraction tomography,'' IEEE Trans. Microwave Theory Tech. **32**, 860–874 (1984).
[45] T. D. Mast, L. M. Hinkelman, M. J. Orr, and R. C. Waag, ''Simulation of ultrasonic pulse propagation, distortion, and attenuation in the human chest wall,'' submitted to J. Acoust. Soc. Am. **106**, 3665–3677 (1999).